2019

Peierls barrier characteristic and anomalous strain hardening provoked by dynamic-strain-aging strengthening in a body-centered-cubic high-entropy alloy

S. Y. Chen
University of Tennessee, Knoxville

L. Wang
University of Tennessee, Knoxville

W. D. Li
University of Tennessee, Knoxville

Y. Tong
University of Tennessee, Knoxville

K. K. Tseng
National Tsing Hua University, Hsinchu, Taiwan

See next page for additional authors

Materials Research Letters

ISSN: (Print) 2166-3831 (Online) Journal homepage: https://www.tandfonline.com/loi/tmrl20

Peierls barrier characteristic and anomalous strain hardening provoked by dynamic-strain-aging strengthening in a body-centered-cubic high-entropy alloy

S. Y. Chen, L. Wang, W. D. Li, Y. Tong, K. K. Tseng, C. W. Tsai, J. W. Yeh, Y. Ren, W. Guo, J. D. Poplawsky & P. K. Liaw

To cite this article: S. Y. Chen, L. Wang, W. D. Li, Y. Tong, K. K. Tseng, C. W. Tsai, J. W. Yeh, Y. Ren, W. Guo, J. D. Poplawsky & P. K. Liaw (2019) Peierls barrier characteristic and anomalous strain hardening provoked by dynamic-strain-aging strengthening in a body-centered-cubic high-entropy alloy, Materials Research Letters, 7:12, 475-481, DOI: 10.1080/21663831.2019.1658233

To link to this article: https://doi.org/10.1080/21663831.2019.1658233

Published online: 27 Aug 2019.

MATER. RES. LETT.
2019, VOL. 7, NO. 12, 475–481
https://doi.org/10.1080/21663831.2019.1658233

MATERIALS RESEARCH LETTERS
Taylor & Francis
Taylor & Francis Group

ORIGINAL REPORT

Peierls barrier characteristic and anomalous strain hardening provoked by dynamic-strain-aging strengthening in a body-centered-cubic high-entropy alloy

S. Y. Chen[a], L. Wang [a], W. D. Li[a], Y. Tong[a], K. K. Tseng[b,c], C. W. Tsai [b,c], J. W. Yeh[b,c], Y. Ren[d], W. Guo[e], J. D. Poplawsky [e] and P. K. Liaw[a]

[a]Department of Materials Science and Engineering, The University of Tennessee, Knoxville, TN, USA; [b]Department of Materials Science and Engineering, National Tsing Hua University, Hsinchu, Taiwan; [c]High Entropy Materials Center, National Tsing Hua University, Hsinchu, Taiwan; [d]X-ray Science Division, Argonne National Laboratory, Argonne, IL, USA; [e]Center for Nanophases Materials Sciences, Oak Ridge National Laboratory, Oak Ridge, TN, USA

ABSTRACT

The temperature effect on the mechanical behavior of the HfNbTaTiZr high entropy alloy (HEA) was investigated at 77–673 K. The decrease of the yield strength with increasing the temperature was mechanistically analyzed by considering contributions from various strengthening mechanisms. An anomalous dependence of strain hardening on temperature was observed and was justified to be caused by dynamic strain aging (DSA) as an extra strengthening mechanism at elevated temperatures. A model was constructed to split the overall strain hardening into forest hardening and DSA hardening, both of which were theoretically quantified at all temperatures considered.

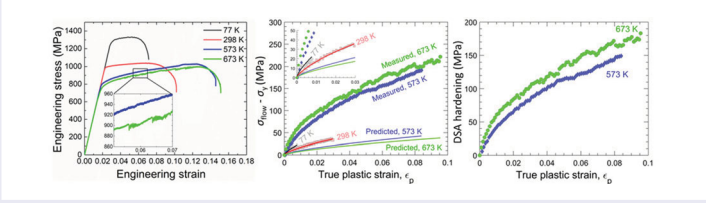

IMPACT STATEMENT

The work quantifies the height of Peierls barriers in the bcc HfNbTaTiZr HEA, and reveals dynamic strain aging as the strengthening mechanism causing the anomalous strain hardening at elevated temperatures.

ARTICLE HISTORY
Received 1 July 2019

KEYWORDS
Strain hardening; temperature dependence; dislocation width; serrated flow; dynamic strain aging

Metal alloys derive their intrinsic yield strengths from lattice resistance to dislocation motion [1]. The lattice friction increase in dilute alloys originates from the elastic interaction between moving dislocations and the strain filed created by discrete solute atoms [1]. Despite this mechanistic sketch breaks down when coming to HEAs due to indistinguishable solvents and solutes, envisaging the complex lattice as an effective medium encompassing solid-solution strengthening still permits us to gauge the resistance of the 'average lattice' to dislocation motion [2]. The effective medium treatment essentially ensures the validity of the Peierls stress in assessing the 'average lattice' friction in complex concentrated alloys. The weaker temperature dependence of yield strengths in face-centered-cubic (fcc) metals than that in body-centered-cubic (bcc) metals implies that bcc metals have narrower dislocation widths than the fcc metals [2–4]. It was reported that equiatomic face-centered-cubic (fcc) alloys belonging to the subsets of the fcc FeNiCoCrMn HEA possessed narrower dislocation widths than pure fcc metals [2,5]. If the same logic prevails, the equiatomic bcc HEAs are anticipated to possess narrower dislocation widths than the equiatomic fcc alloys. This conjecture is examined in the present work by investigating the temperature dependence of the yield strength of the bcc HfNbTaTiZr HEA.

Following yielding, the strengthening in flow stresses (i.e. strain hardening) is taken over by the interaction between moving dislocations and forest dislocations [6]. When deformed at elevated temperatures, dynamic recovery tends to annihilate dislocations and alleviate dislocation interactions, thereby weakening strain

CONTACT W. D. Li wli20@utk.edu Department of Materials Science and Engineering, The University of Tennessee, Knoxville, TN 37996, USA; P. K. Liaw pliaw@utk.edu Department of Materials Science and Engineering, The University of Tennessee, Knoxville, TN 37996, USA

hardening [7]. This fact is reflected on stress–strain curves as the flattening of the plastic portion with increasing the temperature. Such a negative temperature effect on strain hardening holds true for the majority of conventional alloys and recently invented HEAs (e.g. [2,8–10]). Nevertheless, this prevalent scenario may be altered when some other strengthening mechanisms unique to high-temperature deformation set in. For instance, dynamic strain aging (DSA) may arise in certain temperature ranges to offer an extra strengthening mechanism [11,12]. The positive strengthening contribution from DSA may offset or exceeds the temperature-induced softening and lead to greater strain hardening at elevated temperatures. This anomalous temperature dependence of strain hardening is observed in the present bcc HfNbTaTiZr HEA and will be analyzed in depth.

The preparation and processing of the HfNbTaTiZr alloy followed the steps in Ref. [13]. Flat dog-bone tensile specimens with a 19-mm gauge were machined with their longitudinal axes perpendicular to the rolling direction. Following grinding and polishing, the samples have a thickness and gauge section width of $\sim$0.9 and 3.15 mm, respectively. Uniaxial tensile tests were conducted on a Material Test System (MTS) servohydraulic machine at a strain rate of $1 \times 10^{-4}\,s^{-1}$ and temperatures of 77, 298, 573, and 673 K, under the displacement control. At least three tests were repeated for each condition. The cryogenic tests followed the procedure in Ref. [2]. X-ray diffractions were carried out on the 11-ID-C beamline (beam energy 115.27 keV), at Advanced Photon Source (APS) of Argonne National Laboratory. Scanning electron microscopy (SEM: LEO 1525 at 30 keV) was selected to investigate fractographic changes after deformation; cross-sectional transmission electron microscopy (TEM: Zeiss Libra 200 at 200 keV) in scanning TEM (STEM) mode as well as selected area electron diffraction (SAED) patterns were applied to investigate possible second phases. TEM samples were prepared by using focused ion beam (FIB: Zeiss Auriga crossbeam FIB/SEM) lift-out method. The final thinning was conducted using 5 keV Ga+ with a $\pm$ 6° incidence angle between the Ga+ beam and the sample surface for 10 mins to remove FIB-induced damge. Atom probe tomography (APT) experiments were performed at the Center for Nanophase Materials Sciences (CNMS) in the Oak Ridge National Laboratory (ORNL).

Figure 1(a) gives the tensile engineering stress–strain curves of the HfNbTaTiZr HEA tested at temperatures from 77 to 673 K. Analogous to the vast majority of crystalline metals, the increase in temperature intensifies ductility yet brings down the yield stress and flow stress, as shown separately by the symbol plots in Figure 1(b,c). Also noted in Figure 1(a) is that flow serrations take place on the 673 K curves, as revealed by the inset.

A feature in Figure 1(a) that distinguishes this HEA from other crystalline metals and HEAs is that its strain hardening after 298 K seems to enhance as temperature goes high. According to the Hollomon power law, $\sigma = A\varepsilon_p^n$, the strain-hardening exponent, n, for each temperature is computed by performing a $\log\sigma - \log\varepsilon_p$ fit to the true flow stress against the true plastic strain up to necking. n values evaluated at all temperatures are plotted in Figure 1(d). The plot confirms the visual inspection in Figure 1(a): strain hardening first decreases from 77 to 298 K, and then reverts to an ascending trend as the temperature further increases. The decline in strain hardening from 77 to 298 K is somewhat expected. However, its increase from 298 to 673 K is completely counter-intuitive, because strain hardening in most metals, e.g. all subsets of the fcc FeNiCoCrMn HEA [2], is deteriorated by elevating the temperature. This anomaly in strain hardening is intriguing and will be examined in detail shortly.

The specimens failed at 298 and 673 K were selected for fractographic analyses using an SEM. Their side and top views are presented in the first and second columns in Figure 2, respectively. Upon failure, the degrees of macroscopic necking at these two temperatures are rather comparable. Recalling from Figure 1(a,b) that the alloy's ductility indeed increases significantly from 298 to 673 K, we can reason that the intensified strain hardening has already occurred to the alloy at 573 and 673 K compared to that at 298 K so as to postpone the onset of necking instability. This fractographic observation is essentially consistent with the strain-hardening trend reported in Figure 1(a,d). Microscopically, the specimen at 673 K demonstrates more extensive slip lines than that at 298 K, as evidenced by comparing Figure 2(a_3,b_3). Also, much larger dimples of varying sizes are detected in the former than in the latter, as seen from Figure 2(a_4,b_4). All these reaffirm that the alloy at a higher temperature has a manifestation of greater ductility and strain hardening.

The temperature dependence of the yield strength, σ_y, can be analyzed by firstly considering the contributions from all possible strengthening mechanisms,

$$\sigma_y = \sigma_{fr} + \Delta\sigma_{\rho i} + \Delta\sigma_{ss} + \Delta\sigma_{ppt} + \Delta\sigma_{gb}, \qquad (1)$$

where σ_{fr}, $\Delta\sigma_{\rho i}$, $\Delta\sigma_{ss}$, $\Delta\sigma_{ppt}$, and $\Delta\sigma_{gb}$ are the contributions from the lattice friction, initial dislocation density, solid-solution hardening, precipitation hardening, and grain-boundary hardening, respectively. Given that the alloy examined was well annealed, $\Delta\sigma_{\rho i}$ is approximated as zero. $\Delta\sigma_{ppt}$ is treated as zero also considering the absence of precipitates at all temperatures. $\Delta\sigma_{gb}$ is assumed to be zero in light of Ref. [2]. Finally, analogous

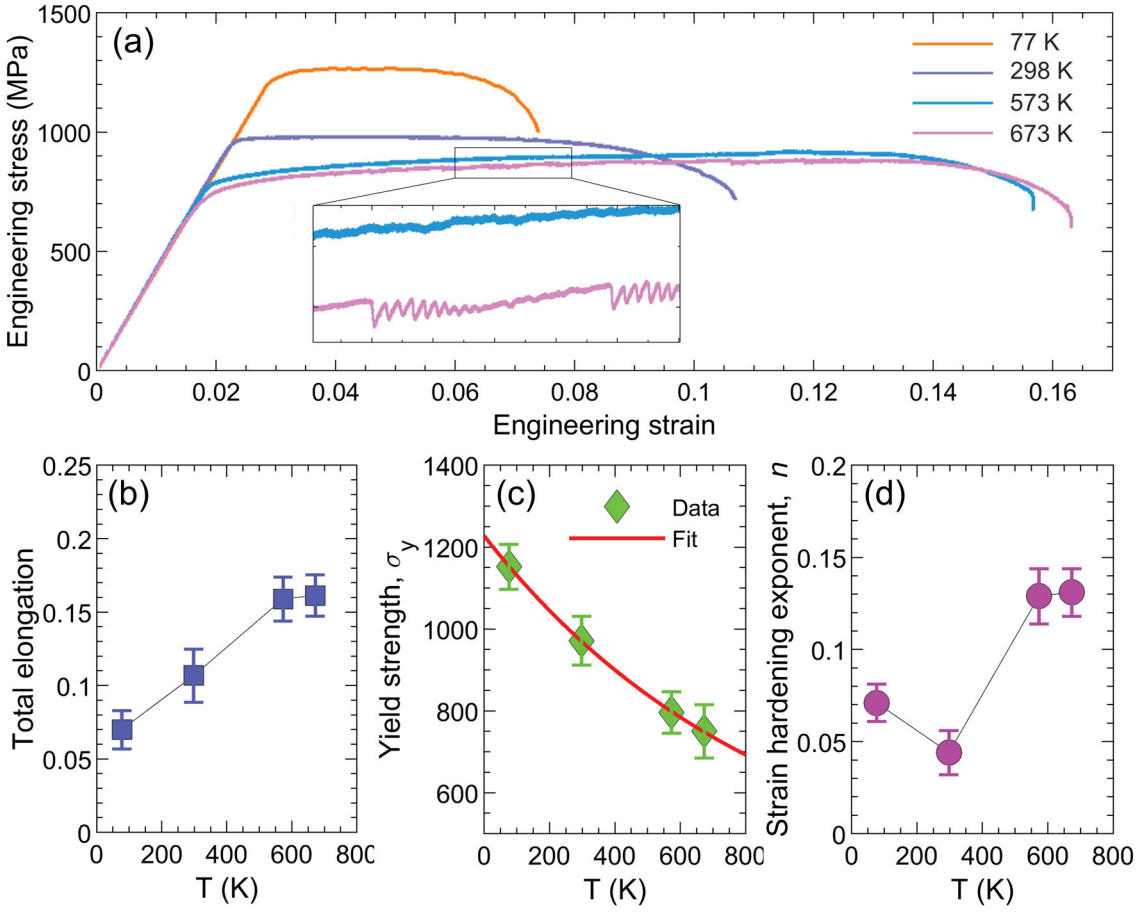

Figure 1. Uniaxial tensile behavior of the bcc HfNbTaTiZr HEAs at 77–673 K. (a) Engineering stress–strain curves. (b) Ductility against temperature. (c) Yield strength against temperature, with the fitting curve by Equation (3). (d) Strain-hardening exponent against temperature.

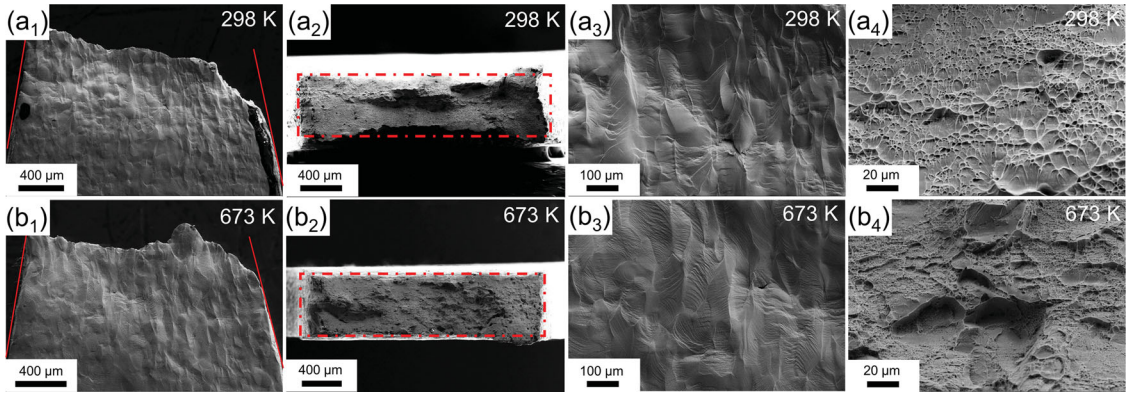

Figure 2. Macroscopic and microscopic fractographs of the HfNbTaTiZr samples failed at ($a_{1\text{-}4}$) 298 K and ($b_{1\text{-}4}$) 673 K.

to Wu et al. [2], $\Delta\sigma_{ss}$ is folded into σ_{fr} to form the average lattice friction $\bar{\sigma}_{fr}$. $\bar{\sigma}_{fr}$ is represented by the Peierls stress, σ_p, and its dependence on temperature is expressed as [2]

$$\sigma_y(T) = \bar{\sigma}_{fr}(T) = \sigma_p = \frac{2G}{1-\nu}\exp\left(\frac{-2\pi\omega_0}{b}\right) \times \exp\left(\frac{-2\pi\omega_0}{b}\alpha T\right), \quad (2)$$

where G is the shear modulus, ν is the Poisson's ratio, ω_0 is the dislocation width at 0 K, b is the magnitude of the Burgers vector, α is a constant, and T is the temperature. Experimentally, the temperature dependence of σ_y may be empirically fitted by the following exponential decay

$$\sigma_y = \sigma_a \exp\left(\frac{-T}{C}\right) + \sigma_b, \quad (3)$$

Table 1. Parameters and their values used in Equations (2) and (3).

Parameter	σ_a (MPa)	C (K)	σ_b (MPa)	ω_0/b	α (K^{-1})
Value	892.8	874.6	334.8	0.74	2.5×10^{-4}

where σ_a, σ_b, and C are all fitting constants. Fitting Equation (3) to the measured σ_y at different temperatures in Figure 1(c) yields the values of three fitting parameters, as listed in Table 1. By examining the functional forms of Equations (2) and (3), it is recognized that $\sigma_a = \frac{2G}{1-\nu}\exp\left(\frac{-2\pi\omega_0}{b}\right)$ and $C = b/2\pi\omega_0\alpha$. With $\sigma_a = 892.8$ MPa, $G = 31$ GPa, $\nu = 0.32$, ω_0/b is calculated to be 0.74, which is expectedly smaller than the dislocation width at room temperature, $\omega_{RT}/b = 0.93 - 0.98$ [14]. Further, with $C = 874.6$ K and $\omega_0/b = 0.74$, α is computed to be 2.5×10^{-4} K^{-1}.

The present results confirm that the bcc HfNbTaTiZr HEA has a narrower dislocation width than the equiatomic fcc solid-solution alloys who have $\omega_0 = b$ [2]. This trend indicates that the former has a stronger Peierls barrier than the latter [15].

Also interesting is the anomalous temperature dependence of the strain-hardening exponent in Figure 1(d) at temperatures greater than 298 K—normally strain hardening of metals drops as temperature increases due to the high-temperature dynamic recovery [2,7,16]. The first thought is that it may be associated with the activation of more slip systems at high temperatures or the change of cross slip. Nonetheless, these factors can be readily ruled out, considering that a temperature increase can cause the same changes in bcc pure metals but still weaken their strain hardening [17]. Then, what is more likely is that some extra hardening mechanism is involved. The first possible extra hardening mechanism is precipitation hardening, likely caused by the high-temperature-promoted precipitation of second phases [18]. The second possible source is the dynamic strain aging (DSA) [19], as clued from the serrated plastic flow in Figure 1(a).

We first examine the likelihood of precipitation hardening. The synchrotron diffractions on the failed specimens at four temperatures are provided in Figure 3(a), from which a bcc phase is identified as the only structure at all temperatures, affirming the nonexistence of second phases in an appreciable amount or large sizes. The possibility of second phases appearing in a small amount or nano sizes is surveyed by conducting TEM and APT analyses at multiple randomly-selected locations on the failed samples. All investigations do not reveal any detectable second phases too, as representatively indicated by the TEM images/diffractions in Figure 3(b,c), also the uniform APT elemental distributions in Figure 3(d). Accordingly, precipitation hardening is eliminated as an extra hardening mechanism.

Up to this point, it is rational to assert that the enhanced strain hardening in the present HEA at temperatures greater than 298 K stems from DSA, an acknowledged strengthening mechanism in alloys [20,21]. In solid-solution alloys without DSA, strain hardening is exclusively attributed to the mutual interaction of mobile dislocations and obstacles (i.e. forest dislocations) [22]. In this case, forest hardening is the only source of strain hardening [22,23], i.e.

$$\Delta\sigma = \sigma_f(\varepsilon_p, T), \tag{4}$$

where $\Delta\sigma$ is the extent of strain hardening defined as the difference between the flow stress and the yield strength, and ε_p is the plastic strain. In the presence of DSA, solute atoms diffuse around dislocations while they are arrested by obstacles for certain time [12,23,24]. This process strengthens the obstacles held on the dislocations and, therefore, provides an additive strengthening on top of the foresting hardening [12,25]. In such a scenario, the extent of strain hardening consists of two contributions, given by

$$\Delta\sigma = \sigma_f(\varepsilon_p, T) + \sigma_{DSA}(\dot{\varepsilon}, T), \tag{5}$$

where $\sigma_{DSA}(\dot{\varepsilon}, T)$ is the temperature- and strain rate-dependent DSA strengthening [26,27].

With the above framework laid out, it is likely to quantify the contribution of forest hardening and DSA hardening to strain hardening in the HfNbTaTiZr HEA at various temperatures. Here we reason that the strain hardening at low temperatures (77 and 298 K) is merely attributed to forest hardening, whereas forest hardening and DSA hardening both constitute the strain hardening at high temperatures (573 and 673 K). The reasoning is on the basis of the contrasting strain-hardening trends at low and high-temperature ranges [c.f., Figure 1(a,d)] as well as the observation of flow serrations at 673 K. Although serrations are absent at 573 K, most likely DAS is still a valid strengthening mechanism at this temperature, considering (1) the alloy at this temperature exhibits similar hardening characteristics to the alloy at 673 K, and (2) the serrated flow is not necessarily always visible upon DSA [27]. The appearance of serrations in the samples tested at 573 K and a loading rate of 1×10^{-5} s^{-1} (not shown) is also a justification of this proposition. Given that forest hardening presents in the alloy at all temperatures, we first attempt to quantify it. According to Ref. [23], forest strengthening can be written as

$$\sigma_f = \omega A \frac{\sqrt{\rho_f}}{b}, \tag{6}$$

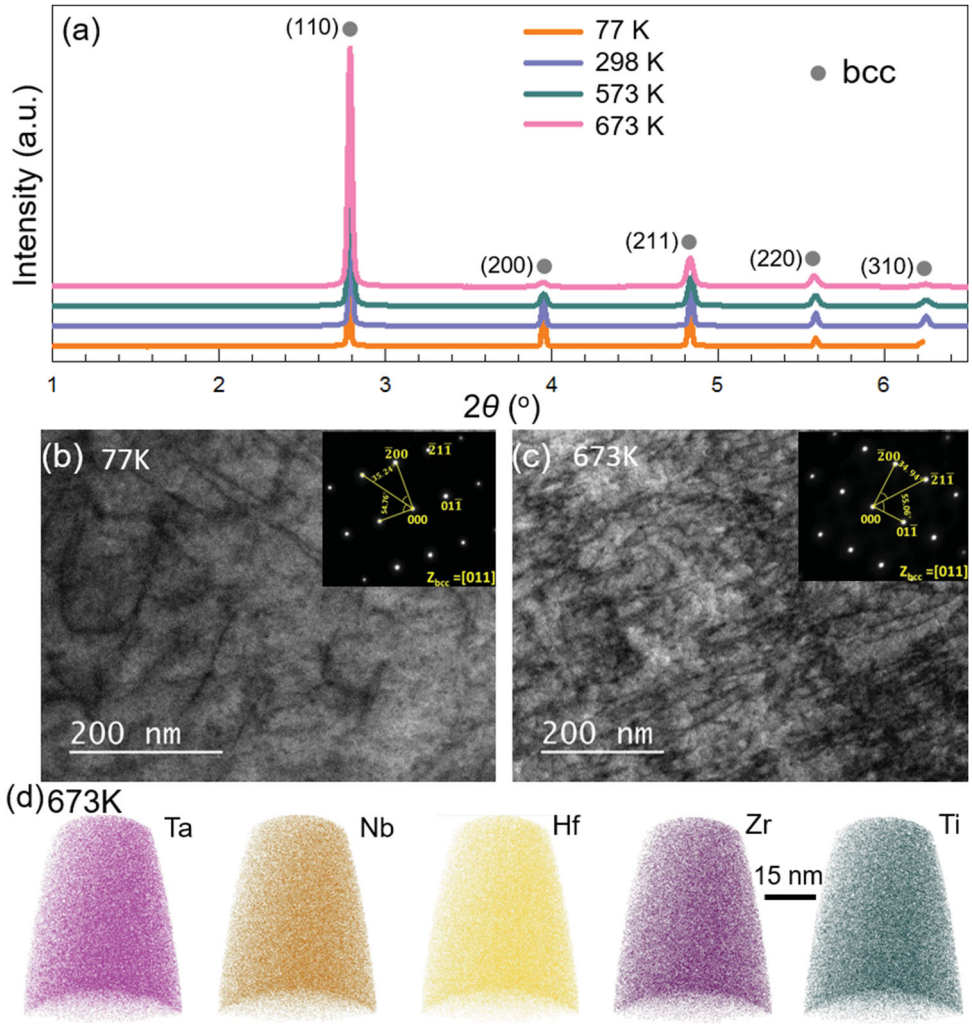

Figure 3. Representative microstructural probing of the failed HfNbTaTiZr HEA. (a) Synchrotron diffractions at 77–673 K. Bright-field STEM images at (b) 77 K and (c) 673 K, with the insets of SAED patterns. (d) APT atom maps at 673 K.

where ω is a constant, ρ_f is the forest dislocation density, and $A = \frac{3Gb^2}{4\pi(1-\nu)}$. Equation (6) essentially has the same functional form as the classical Taylor hardening model [28]. The evolution of the forest dislocation density with the plastic strain follows the general form of [23]

$$\rho_f(\varepsilon_p) = \rho_f^{sat}(1 - \exp(-(\varepsilon_p/\bar{\varepsilon}_p)^p)), \tag{7}$$

where $\bar{\varepsilon}_p$ and p are constants, ρ_f^{sat} is the saturated forest dislocation density at a given temperature. Apparently, ρ_f^{sat} decreases with increasing temperature. Inspired by prior reports [29], the dependence of ρ_f^{sat} on temperature is assumed to follow an exponential decay

$$\rho_f^{sat}(T) = \rho_{f,0}^{sat}\exp(-\zeta T), \tag{8}$$

where $\rho_{f,0}^{sat}$ is the zero-temperature forest dislocation density, and ζ is a constant. Combining Equations (6)–(8), one can obtain the ultimate forest strengthening model as

$$\sigma_f(\varepsilon_p, T) = \xi\frac{A}{b}\sqrt{\exp(-\zeta T)(1 - \exp(-(\varepsilon_p/\bar{\varepsilon}_p)^p))}, \tag{9}$$

where $\xi = \omega\sqrt{\rho_{f,0}^{sat}}$ is a constant. For the HfNbTaTiZr HEA, b and A are determined to be 2.944 Å and 0.6 eV/Å, respectively; ξ, ζ, $\bar{\varepsilon}_p$, and p are adjustable parameters that need to be evaluated by fitting the model to the measurement data.

The extent of strain hardening ($\Delta\sigma = \sigma_{flow} - \sigma_y$) vs. true plastic strain (ε_p) for the HfNbTaTiZr at 77–673 K are provided in Figure 4(a). Given that forest hardening is the only strain-hardening source in the alloy at 77 and 298 K, ξ, ζ, $\bar{\varepsilon}_p$, and p values are determined through a simultaneous fitting of Equation (9) to the strain-hardening curves at 77 and 298 K by meeting an

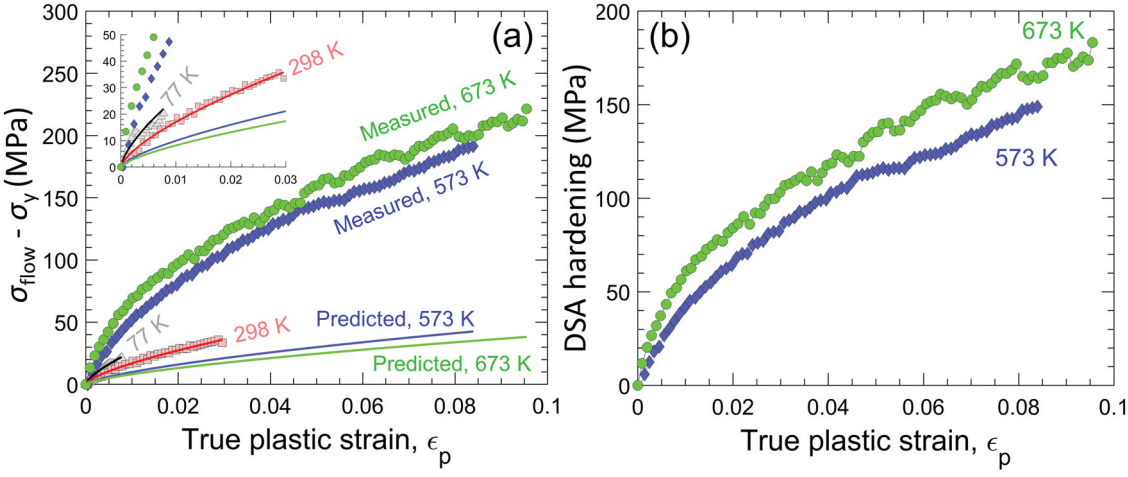

Figure 4. (a) Strain-hardening portion of the flow stress ($\Delta\sigma = \sigma_{flow} - \sigma_y$) vs. true plastic strain (ε_p) at temperatures from 77 to 673 K. The symbols stand for measurements whereas lines are the predictions by the forest hardening model defined in Equations (4) and (9). (b) Estimated DSA hardening at 573 and 673 K.

Table 2. Parameters and their values used in Equation (9) for predicting the foresting hardening at all temperatures.

Parameter	b (Å)	A (eV/Å)	ξ (m^{-1})	ζ	$\bar{\varepsilon}$	p
Value	2.944	0.60	2×10^5	3.9×10^{-3}	0.86	1.38

objective of minimizing

$$wt_{77} \sum_{i=1}^{n} \left(\frac{\Delta\sigma_i^p - \Delta\sigma_i^m}{\Delta\sigma_i^m} \right)^2 + wt_{298} \sum_{j=1}^{k} \left(\frac{\Delta\sigma_j^p - \Delta\sigma_j^m}{\Delta\sigma_j^m} \right)^2,$$

where $wt_{77} = wt_{298} = 0.5$ are the weights of the data sets at 77 and 298 K, n and k are the total numbers of data points at 77 and 298 K, $\Delta\sigma_i^p$, $\Delta\sigma_i^m$, $\Delta\sigma_j^p$, and $\Delta\sigma_j^m$ are the predicted and measured $\Delta\sigma$ for 77 and 298 K. With the best-fit curves at 77 and 298 K shown in Figure 4(a), the parameter values determined are listed in Table 2. It is appropriate to believe that the resulting forest hardening model is applicable to the same alloy at 573 and 673 K. With the parameter values in Table 2, the model in Equation (9) predicts the forest hardening at 573 and 673 K as the blue and green curves in Figure 4(a). Two striking features are noted in Figure 4(a). Firstly, if only looking at the predicted curves, forest hardening weakens, as temperature increases, a trend in line with that in most conventional metals [28] and equiatomic fcc alloys [2]. Secondly, the difference between the measured overall strain hardening and the predicted forest strain hardening at 573 and 673 K is due to the DSA hardening according to Equation (5).

The magnitude of DSA hardening at 573 and 673 K may be estimated by simply subtracting the predicted curves from the measured data in Figure 4(a). The resulting DSA hardening as a function of plastic strain at the two temperatures of 573 and 673 K is graphed in Figure 4(b). The DSA hardening at 673 K is slightly greater than that at 573 K, essentially capturing the observation in Figure 1(a) that the former manifests more pronounced flow serrations than the latter. DSA hardening boosts with increasing plastic strain because larger plastic deformation is inclined to induce more dislocations, thereby expanding the scale of DSA events. The DSA hardening estimated in this way accounts for the integrated effects from both mobile dislocations and forest dislocations. With more rigorous theoretical treatments, the DSA hardening resulting from these two different types of dislocations may be separated [23,30,31], which could be done in future work.

In closing, we would like to point out that our fitting procedure may be made more robust by considering the temperature dependence of the weighting factors as well as using a cross-validation technique.

Disclosure statement

No potential conflict of interest was reported by the authors.

Funding

We are grateful for the financial support of the National Science Foundation of US (DMR-1611180 and 1809640), the U.S. Army Research Office project (W911NF-13-1-0438 and W911NF-19-2-0049) with the program managers, Drs. G. Shiflet, D. Farkas, M. P. Bakas, S. N. Mathaudhu, and D. M. Stepp, in US, and theMinistry of Science and Technology (MOST 107-3017-F-007-003) in Taiwan. APT was conducted at ORNL's Center for Nanophase Materials Sciences (CNMS), which is a U.S. DOE Office of Science User Facility. This research used resources of the Advanced Photon Source, a U.S. Department of

Energy (DOE) Office of Science User Facility operated for the DOE Office of Science by Argonne National Laboratory under Contract No. DE-AC02-06CH11357.

ORCID

L. Wang http://orcid.org/0000-0001-7317-5766
C. W. Tsai http://orcid.org/0000-0003-3072-7916
J. D. Poplawsky http://orcid.org/0000-0002-4272-7043

References

[1] Argon A. Strengthening mechanisms in crystal plasticity. New York: Oxford University Press on Demand; 2008.
[2] Wu Z, Bei H, Pharr GM, et al. Temperature dependence of the mechanical properties of equiatomic solid solution alloys with face-centered cubic crystal structures. Acta Mater. 2014;81:428–441.
[3] Hutchison MM. The temperature dependence of the yield stress of polycrystalline iron. Philos Mag. 1963;8:121–127.
[4] Bechtold JH. Tensile properties of annealed tantalum at low temperatures. Acta Metall. 1955;3:249–254.
[5] Feltham P, Copley GJ. Yielding and work-hardening in alpha-brasses. Acta Metall. 1960;8:542–550.
[6] Dieter GE, Bacon DJ. Mechanical metallurgy. New York: McGraw-hill; 1986.
[7] Abbaschian R, Reed-Hill RE. Physical metallurgy principles. Stamford: Cengage Learning; 2008.
[8] Podolskiy AV, Tabachnikova ED, Voloschuk VV, et al. Mechanical properties and thermally activated plasticity of the Ti30Zr25Hf15Nb20Ta10 high entropy alloy at temperatures 4.2–350 K. Mater Sci Eng A. 2018;710:136–141.
[9] Senkov ON, Wilks GB, Scott JM, et al. Mechanical properties of Nb25Mo25Ta25W25 and V20Nb20Mo20Ta20W20 refractory high entropy alloys. Intermetallics. 2011;19:698–706.
[10] Gopinath K, Gogia AK, Kamat SV, et al. Tensile properties of Ni-based superalloy 720Li: temperature and strain rate effects. Metall Mater Trans A. 2008;39:2340–2350.
[11] Peng K, Qian K, Chen W. Effect of dynamic strain aging on high temperature properties of austenitic stainless steel. Mater Sci Eng A. 2004;379:372–377.
[12] van den Beukel A. Theory of the effect of dynamic strain aging on mechanical properties. Phys Status Solidi (a). 1975;30:197–206.
[13] Chen SY, Tong Y, Tseng KK, et al. Phase transformations of HfNbTaTiZr high-entropy alloy at intermediate temperatures. Scripta Mater. 2019;158:50–56.
[14] Zhao YY, Lei ZF, Lu ZP, et al. A simplified model connecting lattice distortion with friction stress of Nb-based equiatomic high-entropy alloys. Mater Res Lett. 2019;7:340–346.
[15] Joós B, Duesbery MS. The Peierls stress of dislocations: an analytic formula. Phys Rev Lett. 1997;78:266–269.
[16] Poliak E, Jonas J. Initiation of dynamic recrystallization in constant strain rate hot deformation. ISIJ Int. 2003;43:684–691.
[17] Liang R, Khan AS. A critical review of experimental results and constitutive models for BCC and FCC metals over a wide range of strain rates and temperatures. Int J Plast. 1999;15:963–980.
[18] Ardell AJ. Precipitation hardening. Metall Trans A. 1985;16:2131–2165.
[19] Zhang Y, Liu JP, Chen SY, et al. Serration and noise behaviors in materials. Prog Mater Sci. 2017;90:358–460.
[20] Mulford RA, Kocks UF. New observations on the mechanisms of dynamic strain aging and of jerky flow. Acta Metall. 1979;27:1125–1134.
[21] Barat P, Sarkar A, Mukherjee P, et al. Scaling behavior of the Portevin–Le Chatelier effect in an Al-2.5%Mg alloy. Phys Rev Lett. 2005;94:055502.
[22] Madec R, Devincre B, Kubin LP. From dislocation junctions to forest hardening. Phys Rev Lett. 2002;89:255508.
[23] Soare MA, Curtin WA. Solute strengthening of both mobile and forest dislocations: the origin of dynamic strain aging in fcc metals. Acta Mater. 2008;56:4046–4061.
[24] Lebyodkin MA, Brechet Y, Estrin Y, et al. Statistics of the catastrophic slip events in the Portevin–Le Chatelier effect. Phys Rev Lett. 1995;74:4758–4761.
[25] Samuel KG, Mannan SL, Rodriguez P. Another manifestation of dynamic strain ageing. J Mater Sci Lett. 1996;15:1697–1699.
[26] Rizzi E, Hähner P. On the Portevin–Le Chatelier effect: theoretical modeling and numerical results. Int J Plast. 2004;20:121–165.
[27] Hähner P. On the physics of the Portevin-Le Châtelier effect part 1: the statistics of dynamic strain ageing. Mater Sci Eng A. 1996;207:208–215.
[28] Dieter GE, Bacon DJ. Mechanical metallurgy. New York: McGraw-Hill; 1986.
[29] Torganchuk V, Belyakov A, Kaibyshev R. Effect of rolling temperature on microstructure and mechanical properties of 18%Mn TWIP/TRIP steels. Mater Sci Eng A. 2017;708:110–117.
[30] Keralavarma SM, Bower AF, Curtin WA. Quantum-to-continuum prediction of ductility loss in aluminium–magnesium alloys due to dynamic strain aging. Nat Commun. 2014;5:4604.
[31] Tsai C-W, Lee C, Lin P-T, et al. Portevin-Le Chatelier mechanism in face-centered-cubic metallic alloys from low to high entropy. Int J Plasticity. 2019. DOI:10.1016/j.ijplas.2019.07.003